IEEE Access
Multidisciplinary ⋮ Rapid Review ⋮ Open Access Journal

Received 23 July 2024, accepted 30 August 2024, date of publication 4 September 2024, date of current version 12 September 2024.

Digital Object Identifier 10.1109/ACCESS.2024.3454523

RESEARCH ARTICLE

Microwave Bone Imaging: Reconstruction of Anthropomorphic Numerical Calcaneus Phantoms for Bone Diseases Diagnosis

ALESSIA CANNATÀ[1], (Member, IEEE), ADNAN ELAHI[2,3], (Member, IEEE), MARTIN O'HALLORAN[2,3,4], MARCO PASIAN[1], (Senior Member, IEEE), SIMONA DI MEO[1], (Member, IEEE), GIULIA MATRONE[1], (Member, IEEE), AND BILAL AMIN[2,3,4]

[1]Department of Electrical, Computer and Biomedical Engineering, University of Pavia, 27100 Pavia, Italy
[2]Translational Medical Device Laboratory, University of Galway, Galway, H91 TK33 Ireland
[3]Electrical and Electronic Engineering, University of Galway, Galway, H91 TK33 Ireland
[4]School of Medicine, University of Galway, Galway, H91 TK33 Ireland

Corresponding authors: Bilal Amin (bilal.amin@universityofgalway.ie) and Alessia Cannatà (alessia.cannata01@universitadipavia.it)

This work was supported in part by the Erasmus+ Traineeship Programme.

ABSTRACT Microwave Tomography (MWT) is emerging as a potential imaging technique for monitoring bone health due to its ability to determine the dielectric properties of tissues under investigation. Studies have demonstrated a significant dielectric contrast between healthy and diseased human trabecular bones, which suggests that MWT has the potential to detect changes associated with bone disorders. The goal of this study was to assess the numerical reconstruction of an anthropomorphic two-layer (cortical and trabecular bone) calcaneus-shaped phantom, considering both healthy and diseased scenarios. Data were obtained using two different antenna configurations: a 16-antenna circular array and a 24-antenna calcaneus-shaped array. The electromagnetic (EM) inverse problem was solved by employing the Distorted Born Iterative Method (DBIM) in conjunction with the Iterative Method with Adaptive Thresholding for Compressed Sensing (IMATCS). An L_2-based regularization method was applied along with the IMATCS. The results demonstrated that accurate reconstruction of various phantom properties at 1 GHz is feasible even under low signal-to-noise ratio (SNR) conditions. The achieved results suggest that the present approach can provide a good numerical reconstruction of the proposed phantoms both in the circular array and the calcaneus-shaped array scenarios, proving its robustness in distinguishing the overall reference and reconstructed dielectric properties with an average percentage difference of 10.43%. This work revealed the possibility of applying the suggested approach in a new scenario with a realistic phantom in two different antenna-array geometric configurations. In the future, this could be tested in an experimental context to assess the medical conditions of the human bones.

INDEX TERMS Anthropomorphic phantoms, bone health, dielectric properties, Distorted Born Iterative Method (DBIM), Microwave Tomography (MWT).

I. INTRODUCTION

Microwave imaging (MWI) has emerged as a promising diagnostic technology for multiple medical applications [1]. This technology offers several advantages in comparison to existing imaging modalities, including the use of non-ionizing radiations, portability, and cost-effectiveness [1], [2]. MWI has been widely employed in breast cancer detection and several prototypes have been proposed [3], [4], [5], [6], [7], [8], [9], [10]. The underlying principle of MWI lies in the distinction between healthy and tumour tissues based on their dielectric contrast [10], [11], [12].

The associate editor coordinating the review of this manuscript and approving it for publication was Ladislau Matekovits.

Furthermore, MWI has shown promising results for the diagnosis of brain stroke by exploiting the dielectric contrast between ischemic and healthy tissues [13], [14], [15]. In addition to these applications, MWI has also been employed in cardiac imaging [16] and other contexts [17].

Recent studies have explored the possibility of using MWI in monitoring bone health by investigating the dielectric contrast between normal and diseased human bone tissues [18], [19], [20]. Indeed, in [21] the authors reported an average percentage difference between the dielectric properties of the skin and trabecular bone, in terms of relative permittivity and conductivity respectively, of 70% and 56%, while the average percentage difference between the properties of trabecular bone and cortical bone is 48% and 65% respectively, in the frequency range of 0.5–5 GHz.

Among the bone diseases, osteoporosis and osteoarthritis are two common conditions that significantly impact the skeletal system and overall bone health. Osteoporosis, characterized by low bone mass and deterioration of bone tissue, is a major contributor to fractures, especially among the elderly [22]. It is reported that every year almost 8.9 million fractures occur due to osteoporosis worldwide [23]. Conversely, osteoarthritis, a degenerative joint disease, primarily affects the cartilage that cushions the ends of bones in joints [20]. Both pathologies often lead to changes in the microarchitecture of the human trabecular bones.

In current clinical practice, Dual-energy X-ray Absorptiometry (DXA) is commonly used to monitor the health of human bones [18]. However, this method poses long-term risks for patients due to exposure to ionizing radiation [18]. Moreover, this technology does not infer precise information about the quality of the investigated bone, in terms of structural features, composition, and degree of mineralization [23]. Additionally, Quantitative Computed Tomography, while less used compared to DXA, is limited in its use due to equipment and testing costs [24]. While these traditional clinical approaches provide high-resolution images for bone health assessment compared to MWI, however, MWI offers distinct advantages, as already mentioned, making it a viable contender for bone health monitoring. Among those, it has been shown to resolve various bone structures such as cortical and trabecular bone tissues to a resolution that allows for detecting contrast between diseased and healthy bones. Moreover, another good advantage of microwave bone imaging is that of the independence of motion artifatcs from patients' breathing or heartbeat, which is only a minor limitation given the peripheral location of the target organ within the human body.

Studies have reported that the variation in the degree of mineralization of the bones affects the dielectric properties of the bones [18], [20], [25]. The primary goal of MWI for bone health monitoring is not to visualize fine bone structures or small lesions. Instead, it aims to reconstruct the dielectric profile of different diseased bones. In this context, the development of a novel device based on MWI, which requires precisely quantifying the dielectric properties of the bone tissues, may help in the diagnosis of the above-mentioned pathologies.

Microwave Tomography (MWT), a specialized approach of MWI, allows for the estimation of the spatial distribution of the dielectric properties of the human biological tissues (i.e., the relative permittivity (ε_r) and conductivity (σ(S/m))). This involves solving the inverse scattering problem by analysing measured scattered electromagnetic (EM) field data [23]. The EM inverse scattering problem is essentially ill-posed and non-linear and to address this challenge, various EM inverse scattering methods including conjugate gradient techniques [26], [27] and Gauss-Newton (GN) optimization algorithms [28], [29] have been developed.

A well-known conventional technique using a forward solver, i.e., the Distorted Born Iterative Method (DBIM), was instead considered in this paper. This method is based on the approximation of the non-linear inverse scattering problem with an underdetermined set of linear equations [30]. In particular, it is an extended version of the Born and Rytov approximation, which fails in reconstructing a 2D scene in the presence of high contrast between the objects involved in the imaging scenario [31]. This technique does not involve the update of the Green's function at each iteration [32], [33], which could introduce a limitation since the considered scene is meant to deal with biological scenarios where the investigated properties are unpredictable and the dielectric contrast might be high. Within the DBIM method, instead, Green's function is updated at every algorithm iteration. The set of linear equations was solved by using an Iterative Method with Adaptive Thresholding for Compressed Sensing (IMATCS) during each DBIM iteration.

Tomography approaches and particularly the described DBIM imaging method are particularly effective in handling complex imaging problems where the distribution of medium properties is highly nonlinear and can successfully resolve various interfaces providing accurate reconstructions. Thus, even though the human calcaneus normally includes multiple tissues like skin, muscle, fat, cortical bone and trabecular bone, creating several interfaces which complicate the study of the interaction between the biological materials and the EM signals, the proposed approach can overcome this limitation by providing reliable images.

Previous studies have considered bone as a homogenous single tissue, neglecting the difference between cortical and trabecular bone properties [18], [34]. As a matter of fact, within the literature, there is a limited number of works concerning the dielectric properties characterization of the human trabecular bone [2]. The few available studies have reported insufficient data on *in-vivo* human properties. In [18], the authors investigated the *in-vivo* dielectric properties of the human bones of two patients with leg injuries in the frequency range of 900-1700 MHz. Another work has reported the *in-vitro* dielectric properties of porcine bone samples at 1100 MHz [25]. Moreover, in the

same study, good reconstructions of bone phantoms have been reported at 1 GHz. Even in the present work, the numerical reconstructions of the proposed calcaneus phantoms were achieved at this frequency, since it represents a good trade-off between the penetration depth and the image resolution [21], [35], [36].

On the other hand, a small number of attempts to reproduce numerical phantoms with realistic structures have been reported, especially in the field of breast and bone microwave tomography [37], [38], [39], [40], [41].

Since in a realistic clinical scenario, the object to be imaged (i.e., the human calcaneus and the bones overall) is layered and not geometrically regular, in this work, for the first time, we aim to reconstruct the dielectric properties of a more realistic (anthropomorphic) numerical phantom with the DBIM/IMATCS algorithm previously proposed in [31]. In the present study, the phantom was designed as a two-layered calcaneus-shaped structure. The algorithm was tested in two different scenarios: the first investigation adopted a circular antenna configuration, as in [31], with 16 equally-spaced antennas placed around the phantom; in the second scenario, instead, 24 antennas were placed around the phantom along a calcaneus-shaped array.

Previous preliminary investigations have considered a heterogeneous calcaneus-shaped phantom for numerical reconstruction through the first configuration across the proposed method [42], [43] achieving good results even when considering a thin skin layer surrounding the phantom.

The main contributions of this work are threefold. Firstly, a novel two-layered calcaneus-shaped structure is designed, specifically catered to represent the calcaneus in a clinical imaging scenario. This design considers the complex anatomical features of the calcaneus, incorporating an outer layer mimicking the dielectric properties of the human cortical bone and an inner layer mimicking the properties of trabecular bone. Secondly, the work evaluates the effectiveness of DBIM in reconstructing such realistic asymmetrical structures. Lastly, the work compares the performance of an adaptive antenna configuration to the conventional circular antenna array. This investigation aims to determine whether an adaptive antenna configuration could offer improved results when imaging irregularly shaped structures, providing insights into the optimal setup for a prototype calcaneus imaging system. The findings of these numerical analyses have shown that this method is even suitable for the reconstruction of a more complex scenario, with an irregular geometry phantom.

The remainder of the paper is organized as follows: Section II reports the characteristics of the two simulation testbeds and presents the mathematical formulation of the considered approach, describing the DBIM method and the L_2-IMATCS algorithm. Also, the performance metrics used to evaluate the reconstructions are described. Section III presents the results and discussion of the numerical reconstruction of anthropomorphic phantoms. Finally, conclusions are drawn in Section IV.

II. METHOD AND PROCEDURES

A. NUMERICAL BONE PHANTOMS

In this work, a two-layer calcaneus-shaped model was developed and evaluated in a 2D imaging scenario. The outer layer of the model mimics the dielectric properties of the human cortical bone; the inner layer, instead, represents the human trabecular bone. Three different phantoms have been proposed; the outer layer was the same for all of them, while the inner layer was meant to mimic the properties of the normal healthy trabecular bone (phantom P1), the osteoporotic trabecular bone (phantom P2) and the osteoarthritic trabecular bone (phantom P3). In Table 1, the compositions of the phantoms are reported.

TABLE 1. Numerical bone phantoms for simulations.

Phantom label	Outer layer	Inner layer
P1	Cortical bone	Normal trabecular bone
P2	Cortical bone	Osteoporotic trabecular bone
P3	Cortical bone	Osteoarthritic trabecular bone

The two-layer model was then transformed into a 2D EM model according to the single-pole Debye parameters for the two different tissues. The Debye model can be described as:

$$\varepsilon_r(\omega) = \varepsilon_\infty + \frac{\Delta\varepsilon}{1 + j\omega\tau} + \frac{\sigma_s}{j\omega\varepsilon_0} \tag{1}$$

where ε_∞ is the permittivity value at the highest frequency considered, $\Delta\varepsilon$ is the difference between the permittivity value at the lowest and highest frequencies considered, σ_s is the conductivity and τ is the relaxation time constant (assumed to be spatially invariant with the value of 0.5 ps). Table 2 shows the parametric values of the Debye parameters for the considered tissues in the frequency range of 0.5-8.5 GHz [31].

The dielectric properties of normal cortical and trabecular bone tissue were obtained from [44] whereas, the Debye parameters for the osteoporotic and osteoarthritic trabecular bones were set according to the dielectric properties reported in [20].

B. SIMULATION TESTBED

Imaging data were simulated using a Finite Difference Time Domain (FDTD) method with a resolution of 1 mm. As already proposed [1], [28], [29], [30], [38], the FDTD approach was used as a *forward solver* for the inversion procedure in this work. Phantoms were placed in a lossless non-dispersive matching medium ($\varepsilon_\infty = 2.848$, $\Delta\varepsilon = 1.104$, σ_s=0.005 S/m). The simulated measurements were carried out through two different antenna configurations (i.e., circular and calcaneus-shaped array). Regarding the former (Fig.1 (a)), 16-point sources were equally spaced in a circular array around the two-layer phantoms. The latter, instead, involved 24-point sources, which were manually placed following the same shape as the bone model (Fig.1 (b)). The specific number of antennas used in both the array configurations (i.e., 16- and 24-point sources antennas respectively)

TABLE 2. Dielectric properties of bone tissues.

Tissue	Single-pole Debye Parameters			Dielectric properties @ 1 GHz	
	ε_∞	$\Delta\varepsilon$	σ_s (S/m)	ε'	σ (S/m)
Cortical bone	8.75	4	0.01	12.39	0.0736
Normal trabecular bone	14	7	0.1	20.43	0.2125
Osteoporotic trabecular bone	16	3	0.12	18.73	0.1677
Osteoarthritic trabecular bone	24	5	0.1	28.55	0.1795

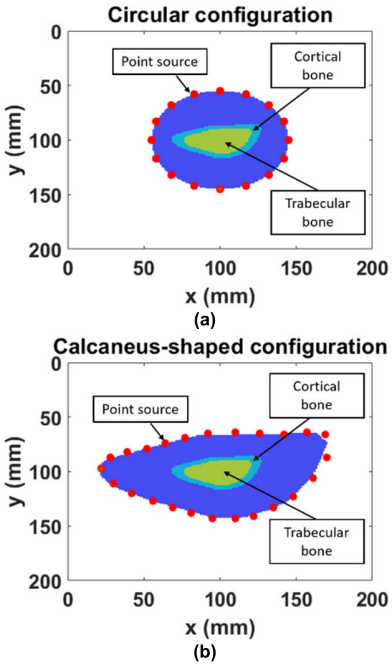

FIGURE 1. Circular (a) and calcaneus-shaped (b) simulation testbeds.

has been chosen as a result of an investigation on the optimum configuration to image the proposed phantoms. We observed that these proposed configurations gave the best results in terms of qualitative reconstructions and quantitative performance metrics. The reconstructions in circular array configurations have been performed by using several antennas ranging from 9 to 16. For what concerns the calcaneus-shaped configuration, we needed to start the investigation by placing at least 18 antennas to reconstruct the target, probably due to the more geometrically complex scenario. We finally chose 24 antennas even to compare our results with [37]. In both cases, the point sources sequentially illuminated the phantoms with a modulated wideband (i.e., 2 GHz) Gaussian pulse, with a central frequency of 1 GHz. Only one recorded EM signal for each transmit-receive antenna pair was considered for the reconstructions (i.e., N(N-1)/2 signals, where N stands for the number of point sources) for a total of 120 signals for the simulations related to the circular configuration and 276 signals for those related to the calcaneus-shaped configuration.

C. DBIM APPROACH

The EM inverse scattering problem is inherently ill-posed (i.e., there are fewer measurements compared to unknowns) and non-linear. The non-linearity arises from the heterogeneity of the target [29] and necessitates non-linear methods for estimating the dielectric properties using the scattered field within the desired frequency range. A graphical description of the imaging scenario is given in Fig. 2. The imaging domain volume (V) is illuminated by an EM field from a known EM source. This approach aims to reconstruct the unknown complex dielectric permittivity of the object to be imaged (Ω) starting from measurements related to one or more observation points outside V.

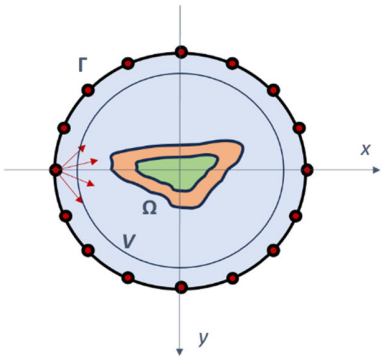

FIGURE 2. MWI Scenario. Γ represents the array with the EM sources (here the circular configuration is shown), *V* is the imaging domain volume while Ω is the object to be imaged.

In this work, the DBIM approximation has been employed to linearize the EM scattering wave equation by replacing the total EM field (i.e., E_{total}) with the known incident field (i.e., E_{inc}), which is estimated at each iteration of the algorithm in the presence of a known background. The computation of the Green's function (i.e., $G_{background}$) is required too, which can be recovered by a *forward solution*. The EM scattered field (i.e., E_{scat}) at measurement point r and angular frequency ω can be expressed as:

$$E_{scat}(r,\omega) = E_{total}(r,\omega) - E_{inc}(r,\omega) \quad (2)$$

$$= \omega^2 \mu \int_V G_{background}\left(r, r', \omega\right) C_f(r', \omega) E_{total}\left(r', \omega\right) dr' \quad (3)$$

where V represents the volume and C_f is the contrast function. The EM scattered equations obtained from this computation are then inverted to get an approximate solution of the contrast between the target region and the current estimation of the background profile (*inverse solution*) [31]. The main principle of the DBIM method relies on updating the background dielectric profile by alternating *forward* and *inverse* solutions until reaching convergence [29].

D. IMATCS ALGORITHM

In EM inverse scattering problems, accurately manipulating the measurements matrix is crucial for recovering the

underlying signals. However, this process is not straightforward [30]. A matrix transformation is required at each DBIM iteration for the unknown complex permittivity vector to make it sparse. The IMATCS algorithm is employed to find the *inverse solution*. As a thresholding approach, it is based on a-priori information, which could be unavailable in many medical applications. Therefore, it relies on adaptive thresholding, where the threshold value is decreased exponentially at each DBIM iteration [24]. The IMATCS algorithm solves the contrast function based on a set of measurements, as displayed below:

$$y = Ax \tag{4}$$

where y is the residual measurement data vector, A is the measurement matrix (with dimensions $m \times n$ ($m < n$),), which relies on E_{inc} and $G_{background}$ from (2)-(3) and it is updated at each DBIM iteration, and x is the unknown dielectric contrast function. The problem displayed in (4) is then solved as follows:

$$\min_x ||y - Ax||_2^2 + \xi ||x||_0 \tag{5}$$

where the solution, applying the adaptive IMATCS method, can be expressed as:

$$x_{j+1} = T_0 e^{-ti}(x_j + \xi A^*(y - Ax_j)) \tag{6}$$

where A^* is the conjugate transpose of A, ξ refers to the convergence of the method, T_0 is the initial threshold value, x_j is the unknown vector, t is the threshold step size and j is the iteration number. The initial value of the algorithm displayed in (6) is null (i.e., $x_0 = 0$). The following values of x_j are retrieved after an optimal number of IMATCS iterations. This method allows for the recovery of the unknown x_j without a-priori information about the signal.

However, the measured data is non-linear and is approximated as linear in this specific application, which may result in instability and divergence of the IMATCS algorithm [31]. To ensure a more stable recovery of the contrast function during each iteration of IMATCS, an L_2-regularized L_0-minimization approach is adopted, as suggested in a previous study [30]. Thus, the problem shown in (5) can be expressed as:

$$\min_x ||y - Ax||_2^2 + \xi_1 ||x||_0 + \xi_2 |\, |x| \,|_2^2 \tag{7}$$

where the solution is given by:

$$x_{j+1} = (1 + \xi_2)^{-1} T_0 e^{-ti} \left(x_j + \xi_1 A^* \left(y - Ax_j\right)\right) \tag{8}$$

This kind of minimization/regularization approach is strongly influenced by the choice of the threshold value which may not lead to convergence. Nonetheless, it ensures a more stable and robust recovery of the unknown variables x_j.

E. IMATCS PARAMETERS SELECTION

As previously stated, selecting appropriate regularization parameters is crucial to achieving the optimal solution for the unknown contrast function. At this stage, it is fundamental to properly set the ξ_1 and ξ_2 convergence parameters, as well as the initial threshold value T_0, the threshold step size t and the maximum number of iterations of the IMATCS algorithm. In particular, since ξ_1 should satisfy the following condition:

$$0 < \xi_1 < 2 / \Upsilon_{max}(AA^*) \tag{9}$$

where $\Upsilon_{max}(AA^*)$ represents the maximum of the eigenvalues of the product AA^*, it has been chosen as:

$$\xi_1 = 1.9 / \Upsilon_{max}(AA^*) \tag{10}$$

The other convergence parameter ξ_2 has been set equal to 0.005 for the reconstruction of all the numerical phantoms. The value of the initial threshold T_0, instead, was chosen empirically for each of the simulations by varying the employed phantom (i.e., P1, P2 or P3) and the physical antenna configuration (i.e., circular or calcaneus-shaped array). The overall value has been set ranging from 125-150 depending on the quality of the single reconstruction. The threshold step size t was set at 0.01, while the number of IMATCS iterations was set at 5 since this value has proved to be a good trade-off between the computational time and the performance of the overall algorithm.

F. EVALUATION OF THE PERFORMANCE

To quantify the performance of the algorithm, two different metrics were computed. The first one, the Normalized Root Mean Square Error (NRMSE), is defined as:

$$\text{NRMSE} = \left|\left|\varepsilon_r(f) - \varepsilon_r^*(f)\right|\right|_{L^2}^2 \Big/ ||\varepsilon_r(f)||_{L^2}^2 \tag{11}$$

where $\varepsilon_r(f)$ is the complex permittivity profile of reference bone dielectric properties, and $\varepsilon^*{}_r(f)$ is the complex permittivity profile of reconstructed bone dielectric properties. The other metric is the Structural Similarity Index (SSIM), which aims to estimate the structural similarity between the reconstructed and reference bone dielectric properties by comparing two images at a time, considering parameters including luminance and contrast [45]. These scalar metrics have been calculated separately for both the real (ε') and imaginary (ε'') parts of the reference and reconstructed complex permittivity profiles of the phantoms.

III. RESULTS AND DISCUSSION

A. NUMERICAL RECONSTRUCTION OF PHANTOMS P1, P2, P3

This section presents the numerical results obtained by the L_2-IMATCS approach for bone dielectric properties' reconstruction using dielectrically informed numerical models. The reconstruction of phantoms P1 (Fig. 3 and Fig. 6), P2 (Fig. 4 and Fig. 7) and P3 (Fig. 5 and Fig. 8) through the described approach within the two different simulation testbeds (i.e., the circular and the calcaneus-shaped antenna configuration) are shown at 1 GHz. The choice of the frequency for image reconstruction was inspired by [21], where the authors investigated the optimum frequency band for bone imaging application considering calcaneus as the

imaging scenario. The authors used a planar layered model of the calcaneus and demonstrated that the most appropriate frequency range for the bone imaging application is 0.6 - 1.9 GHz. Moreover, the authors demonstrated that the penetration depth of EM waves significantly reduced beyond 3 GHz, making it not feasible to distinguish the different tissues of the human calcaneus. Hence, frequencies less than 3 GHz should be considered when designing an MWI system for bone imaging applications [21]. This allows to obtain an overall penetration depth of nearly 5 cm, as reported in [46], which is considered sufficient for this kind of application. The penetration depth is indeed inversely proportional to the dielectric permittivity of a biological tissues. The main issues, thus, are related to the penetration of the EM wave through skin and muscles, which have higher dielectric properties compared to the other tissues involved in the anatomical region of interest. Nonetheless, the external location within the body of the human calcaneus, its biological composition and dimension prove the feasibility of this analysis at microwave frequencies.

As previously described, the employed numerical phantoms have been designed as 2D calcaneus-shaped structures including two different layers. Although it is known that bone tissues are anisotropic and heterogeneous and this might constitute a limitation in accurately modeling their properties, to date no study in the literature has yet quantified any relation between the heterogeneity of bone tissue and their dielectric properties. For this reason, the proposed phantom was constructed and numerically modelled according to the existing techniques provided in the literature, which proved accurate representation of bone properties in imaging studies [18], [19], [30]. Particularly, in this study, cortical and trabecular regions have been modeled separately as distinct homogeneous materials since the main aim was to capture the average dielectric behaviour and detect any significant changes indicative of disease. Therefore, the adopted simplification can be considered as a reasonable approximation for bone disease monitoring application.

The dielectric properties of the cortical bone tissue have been assigned to the outer layer, while the inner layer was meant to mimic the trabecular bone tissue. The main difference among the three phantoms relies on the properties of the trabecular tissue, reproducing respectively a healthy (i.e., P1: normal trabecular bone) and a diseased scenario (i.e., P2: osteoporotic trabecular bone and P3: osteoarthritic trabecular bone). As shown in the figures, in each of the reconstructions, the target (i.e., the trabecular bone) is correctly positioned in the expected region (i.e., the red dotted line in the reconstructed images). The DBIM algorithm was found to converge after one iteration. Therefore, the visual reconstruction results are reported for the first DBIM iteration.

As can be noticed from Figures 5 and 8, when dealing with phantom P3, the shape of the reconstructed object is conserved but the dimension is larger than the reference object. For what concerns the reconstructions of P1 and P2 the method seems to perform well both in terms of the reconstructed dielectric properties and geometric features.

This issue concerning the reconstruction of P3 could be related to the high value of the dielectric properties of the osteoarthritic trabecular bone. The best reconstructions were achieved for the P2 (i.e., osteoporotic) phantom. Indeed, the osteoporotic trabecular bone is the one with the lowest dielectric properties, suggesting that this approach works better in contexts with lower contrast between the properties of cortical and trabecular bones. However, the encountered limitation might be resolved by adaptively changing the threshold of the IMATCS algorithm and optimizing the parameters of the whole method.

The overall findings demonstrate that adopting an adaptive antenna configuration instead of a circular antenna array does not offer significant benefits as the DBIM with L_2-IMATCS algorithm can handle complex imaging scenarios regardless of the antenna configuration.

B. QUANTITATIVE METRICS RESULTS

Two performance metrics (i.e., NRMSE and SSIM) have been calculated as previously described to assess the quantitative performance of the proposed DBIM/IMATCS imaging algorithm. Table 3 shows the results in terms of the mentioned metrics in a non-noisy environment. The reported values suggest that the proposed method is suitable to properly reconstruct such complex-geometry scenarios with both the adopted antenna configurations, reaching comparable performance as in [31], where simplistic versions of the phantoms proposed in this present work have been employed.

The NRMSE has been estimated by comparing the reference and reconstructed properties of the phantoms inside the whole imaging region V. This may explain the achieved values in terms of error, which are still acceptable considering the complex geometry of the phantoms. The SSIM, instead, has been calculated within the only trabecular target region. As can be noticed from Table 3, a slight decrease in the performance occurs in the cases related to the calcaneus-shaped antenna configuration, due to the complexity and the irregularity of the scenario.

TABLE 3. NRMSE and SSIM between original and reconstructed phantoms without noise.

		Circular array			Calcaneus-shaped array		
		P1	P2	P3	P1	P2	P3
NRMSE	ε'	0.151	0.114	0.316	0.318	0.297	0.397
	ε''	0.313	0.357	0.497	0.376	0.286	0.402
SSIM	ε'	0.995	0.994	0.987	0.984	0.982	0.977
	ε''	0.998	0.998	0.997	0.994	0.993	0.991

C. IMPACT OF SNR ON THE RECONSTRUCTED PROPERTIES

MWT is highly sensitive to both noise and artifacts due to the nature of the inverse scattering problem to be solved. Noise from measurements and system imperfections can

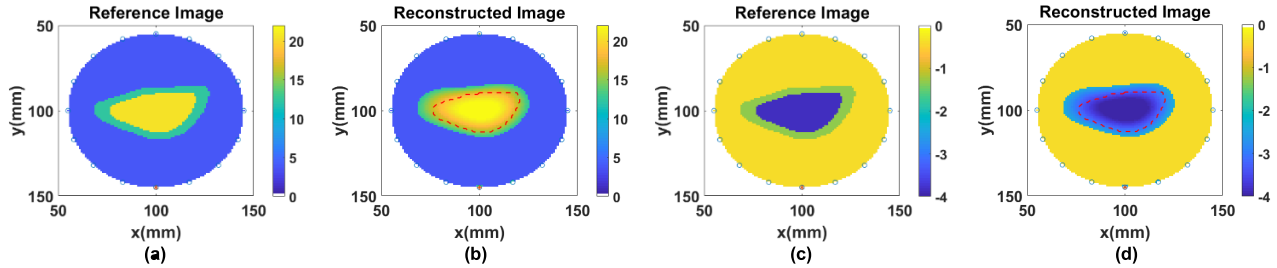

FIGURE 3. Real and imaginary part ((a), (b) and (c), (d), respectively), of the complex dielectric permittivity of reference and reconstructed P1 (cortical + normal trabecular) bone phantom through the 16-antenna circular testbed. The dashed red curves in (b) and (d) represent the reference profiles.

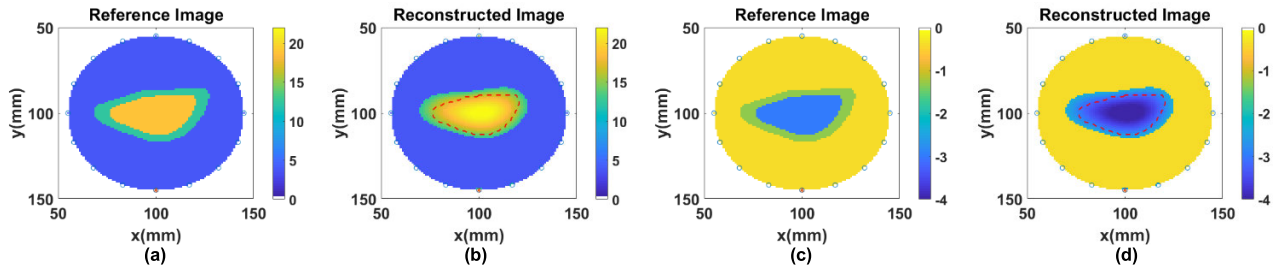

FIGURE 4. Real and imaginary part ((a), (b) and (c), (d), respectively), of the complex dielectric permittivity of reference and reconstructed P2 (cortical + osteoporotic trabecular) bone phantom through the 16-antenna circular testbed. The dashed red curves in (b) and (d) represent the reference profiles.

degrade image quality, while inverse problem artifacts and nonlinear effects can introduce significant artifacts. Effective management of these factors is crucial for achieving reliable reconstructions in MWT.

To make the conditions as realistic as possible, the measured data were corrupted by Additive Gaussian Noise (AWGN). Therefore, the performances in terms of NRMSE were also analyzed by varying the signal-to-noise ratio (SNR) from 20 dB to 60 dB.

The results of this investigation are reported in Tables 4 and 5. The displayed NRMSE values suggest that the developed method performs well even in the case of low SNR values. Thus, this analysis proved the robustness of the DBIM/IMATCS imaging algorithm in the presence of noise.

TABLE 4. NRMSE between original and reconstructed bone phantoms for the real part of complex permittivity, by varying the noise level.

SNR (dB)	Circular array			Calcaneus-shaped array		
	P1	P2	P3	P1	P2	P3
20	0.172	0.145	0.359	0.363	0.300	0.370
30	0.153	0.112	0.405	0.345	0.298	0.367
40	0.149	0.122	0.372	0.377	0.328	0.394
50	0.176	0.121	0.392	0.317	0.297	0.371
60	0.160	0.126	0.399	0.331	0.297	0.372

D. HISTOGRAM ANALYSIS

Additionally, in this work, a histogram-based analysis was carried out. The distribution of the reconstructed real part of the complex permittivity value was computed among each pixel within the target region. As shown in Figure 9 and Figure 10, the reconstruction of P3 was the most challenging, especially for the calcaneus-shaped antenna configuration: the reference value for the osteoarthritic trabecular bone in terms of the real part of the complex permittivity is almost 29, where the properties of almost half (i.e., 49%) of the reconstructed pixels fall into values ranging between 20 and 22.

Nevertheless, the qualitative visual reconstruction of this phantom for both the simulation testbeds and the corresponding performance metrics shows promising results, especially in terms of SSIM. The reason for these slightly low values for P3, as already explained, can be related to the fact that osteoarthritic bone has higher dielectric properties compared to normal and osteoporotic ones. Therefore, due to the higher contrast between the cortical and the trabecular bone regions, the reconstruction is less accurate.

TABLE 5. NRMSE between original and reconstructed bone phantoms for the imaginary part of complex permittivity, by varying the noise level.

SNR (dB)	Circular array			Calcaneus-shaped array		
	P1	P2	P3	P1	P2	P3
20	0.314	0.386	0.409	0.399	0.277	0.406
30	0.320	0.361	0.332	0.396	0.276	0.430
40	0.315	0.399	0.386	0.417	0.339	0.427
50	0.348	0.397	0.378	0.380	0.277	0.396
60	0.335	0.409	0.362	0.378	0.276	0.398

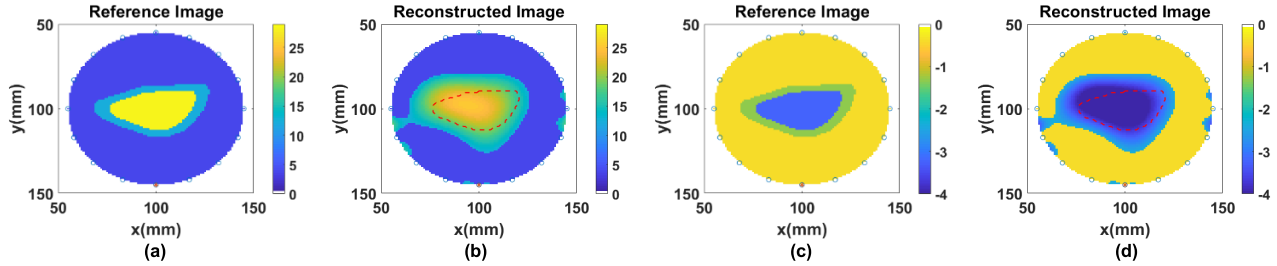

FIGURE 5. The real and imaginary parts ((a), (b) and (c), (d), respectively) of the complex dielectric permittivity of reference and reconstructed P3 (cortical + osteoarthritic trabecular) bone phantom through the 16-antenna circular testbed. The dashed red curves in (b) and (d) represent the reference profiles.

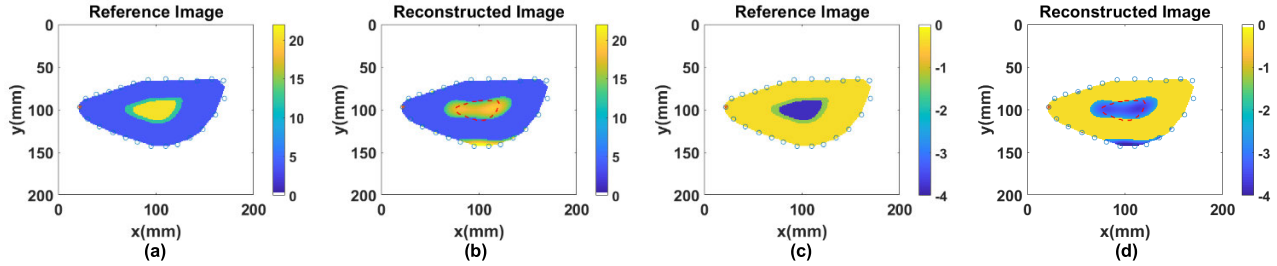

FIGURE 6. The real and imaginary parts ((a), (b) and (c), (d), respectively) of the complex dielectric permittivity of reference and reconstructed P1 (cortical + normal trabecular) bone phantom through the 24-antenna calcaneus-shaped testbed. The dashed red curves in (b) and (d) represent the reference profiles.

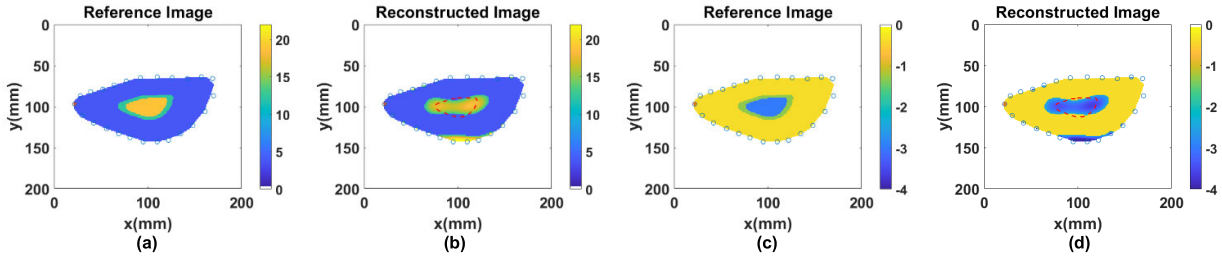

FIGURE 7. The real and imaginary parts ((a), (b) and (c), (d), respectively) of the complex dielectric permittivity of reference and reconstructed P2 (cortical + osteoporotic trabecular) bone phantom through the 24-antenna calcaneus-shaped testbed. The dashed red curves in (b) and (d) represent the reference profiles.

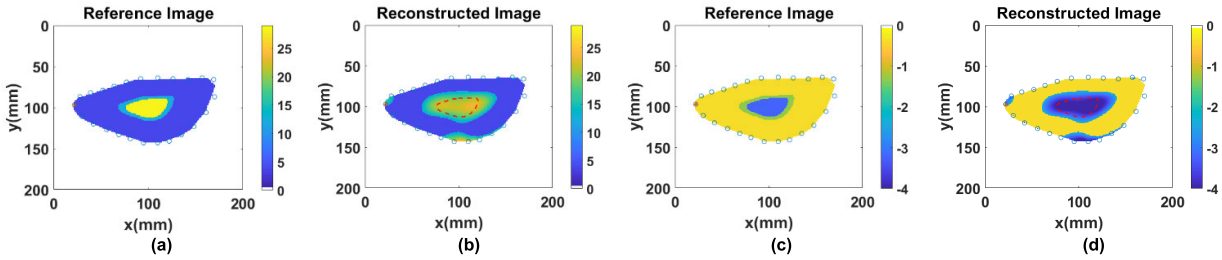

FIGURE 8. The real and imaginary parts ((a), (b) and (c), (d), respectively) of the complex dielectric permittivity of reference and reconstructed P3 (cortical + osteoarthritic trabecular) bone phantom through the 24-antenna calcaneus-shaped testbed. The dashed red curves in (b) and (d) represent the reference profiles.

E. ROBUSTNESS OF THE L_2-IMATCS ALGORITHM FOR RECONSTRUCTION OF P1, P2, P3

To evaluate the robustness of the proposed imaging algorithm, the peak values of the reference and the reconstructed numerical bone properties have been investigated. In Fig. 11, the peak values comparing the reference and reconstructed values of the trabecular bone tissue across the two simulation testbeds are reported. In this analysis, the different physical configurations of the antennas have been considered, to assess whether they could have affected the obtained reconstructions. As can be noticed, regardless of the kind of scenario (i.e., normal, osteoporotic, osteoarthritic) and the antenna configuration, the peak values within the trabecular bone region related to the reconstructed imaginary part of the complex permittivity are higher than the reference.

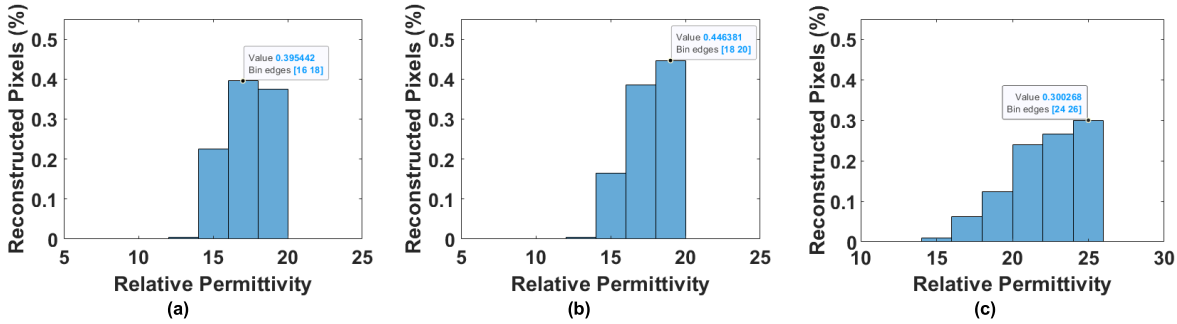

FIGURE 9. Distribution of reconstructed real part of complex permittivity of (a) bone phantom P1, (b) bone phantom P2, (c) bone phantom P3 at 1 GHz for the circular array testbed.

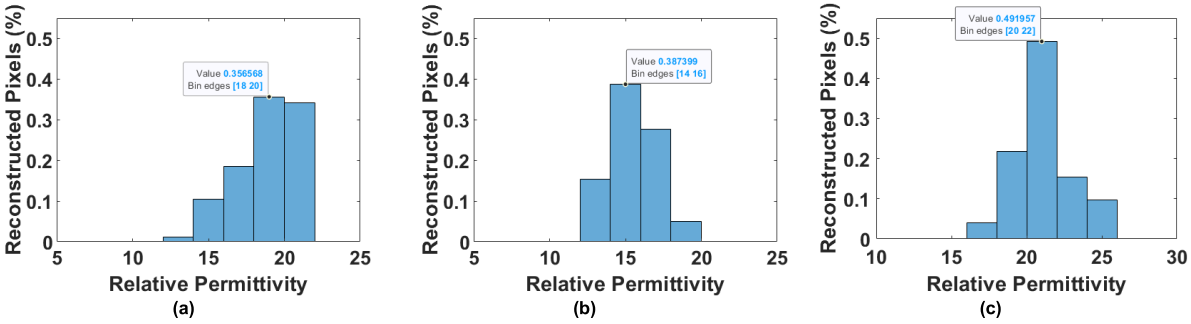

FIGURE 10. Distribution of reconstructed real part of complex permittivity of (a) bone phantom P1, (b) bone phantom P2, (c) bone phantom P3 at 1 GHz for the calcaneus-shaped array testbed.

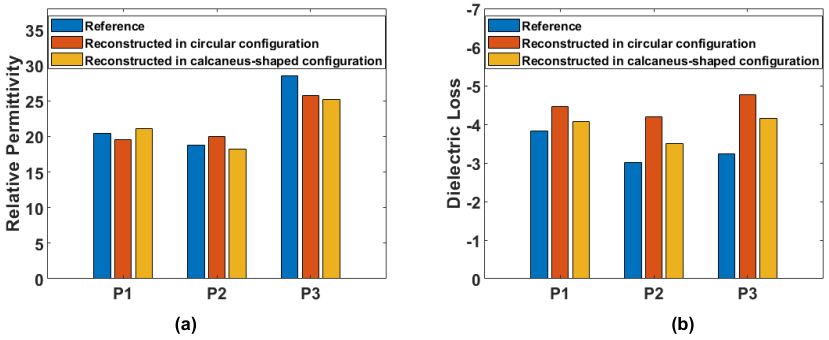

FIGURE 11. Peak values of the (a) real and (b) imaginary part of complex permittivity of reference and reconstructed bone phantoms at 1 GHz.

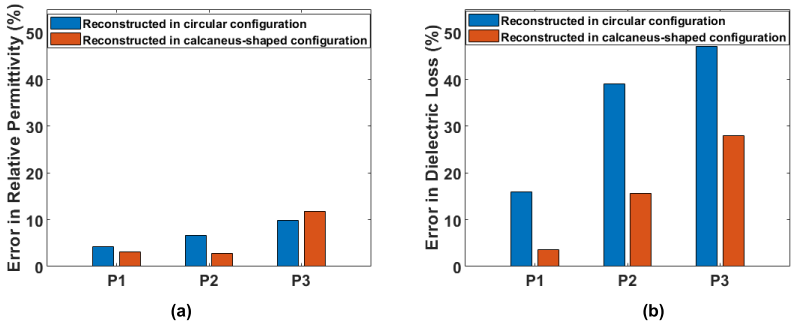

FIGURE 12. Relative percentage error between peak values of the (a) real and (b) imaginary part of complex permittivity of reference and reconstructed bone phantoms at 1 GHz.

The greatest percentage difference between the reference and reconstructed peak values, in terms of the real part of complex dielectric permittivity, has been obtained within the reconstruction of P3, which was expected according to the

previous results. A difference of 11.8% has been reported between the reference osteoarthritic trabecular tissue and the reconstructed one in the calcaneus-shaped antenna configuration. Nonetheless, the average percentage difference between the overall reference and reconstructed real part of the peak values of the phantoms is 6.41%, which suggests that the method can perform well varying either the simulation testbed or the kind of phantom. In Figure 12, both the relative percentage errors for the real and the imaginary part between the reference and reconstructed peak values are shown. As can be noticed in Fig. 12 (b), for all the employed phantoms the error is lower when the calcaneus-shaped configuration is considered compared to the cases related to the circular configuration, proving the robustness of the proposed method even though a more geometrically complex antenna configuration. The higher value of the error in terms of reconstructed peak values, particularly within the circular configuration, might be due to the set threshold, which was specifically tailored to produce good results in terms of the shape and dimension of the reconstructed scene rather than to reach the exact target value of the investigated region.

IV. CONCLUSION

This work has provided a numerical evaluation of an MWT algorithm in a realistic 2D imaging scenario. The phantoms under test have been designed as a two-layered calcaneus-shaped model. Both a healthy and a diseased context have been considered. The simulated data were generated using two different antenna configurations. The first circular configuration was evaluated in a previous study employing a simpler phantom consisting of a two-layered circular structure. In contrast, the second configuration, which had a calcaneus-shaped array, was tested for the first time in this current work. The dielectric properties of the phantoms were reconstructed at 1 GHz using a DBIM approach combined with an L_2-IMATCS algorithm, which has shown promising results in several studies. The results of the present work show that it is possible to extend this method to a more complex scenario involving a realistic phantom. The method proved its efficacy in accurately reconstructing the dielectric properties of the phantom, specifically designed to mimic the complex anatomical structure of the human calcaneus. Moreover, the results provided by the calcaneus-shaped simulation testbed suggest that this method is robust in terms of changes referred to the spatial configuration of the antennas.

The reconstructions of the phantoms P1, P2, and P3 have shown that the normal, osteoporotic and osteoarthritic bones can be accurately distinguished based on their reconstructed complex permittivity profiles.

Future studies may investigate the performance of the described approach in experimental scenarios involving tissue-mimicking phantoms.

Another challenge could be to add the skin layer to the numerical model to evaluate its influence on the reconstruction of the complex dielectric profiles. Even though the skin is generally thin (less than 2 mm) some studies revealed that retrieving its properties is a challenging topic.

Some investigations will be needed as well in terms of the employed matching medium. In this work a loss-less, non-dispersive matching medium was adopted. It could be interesting to explore lossy materials instead, since it may address the limitations posed by signal perturbations and noise as already observed in previous studies concerning phantom for breast imaging.

Finally, future studies will focus on the implementation of the proposed approach to more realistic experimental imaging scenarios involving 3D anatomically realistic bone phantoms tested within the MWI system.

REFERENCES

[1] R. Scapaticci, P. Kosmas, and L. Crocco, "Wavelet-based regularization for robust microwave imaging in medical applications," *IEEE Trans. Biomed. Eng.*, vol. 62, no. 4, pp. 1195–1202, Apr. 2015.
[2] B. Amin, M. A. Elahi, A. Shahzad, E. Porter, B. McDermott, and M. O'Halloran, "Dielectric properties of bones for the monitoring of osteoporosis," *Med. Biol. Eng. Comput.*, vol. 57, no. 1, pp. 1–13, Jan. 2019.
[3] T. M. Grzegorczyk, P. M. Meaney, P. A. Kaufman, R. M. Diflorio-Alexander, and K. D. Paulsen, "Fast 3-D tomographic microwave imaging for breast cancer detection," *IEEE Trans. Med. Imag.*, vol. 31, no. 8, pp. 1584–1592, Aug. 2012.
[4] E. Porter, M. Coates, and M. Popovic, "An early clinical study of time-domain microwave radar for breast health monitoring," *IEEE Trans. Biomed. Eng.*, vol. 63, no. 3, pp. 530–539, Mar. 2016.
[5] A. Fasoula, L. Duchesne, B. M. Moloney, J. D. Gil Cano, C. Chenot, B. L. Oliveira, J.-G. Bernard, S. M. Abd Elwahab, and M. J. Kerin, "Pilot patient study with the wavelia microwave breast imaging system for breast cancer detection: Clinical feasibility and identified technical challenges," in *Proc. 14th Eur. Conf. Antennas Propag. (EuCAP)*, Mar. 2020, pp. 1–5.
[6] S. Di Meo, G. Matrone, and M. Pasian, "Experimental validation on tissue-mimicking phantoms of millimeter-wave imaging for breast cancer detection," *Appl. Sci.*, vol. 11, no. 1, p. 432, Jan. 2021.
[7] M. T. Bevacqua, G. G. Bellizzi, T. Isernia, and L. Crocco, "A method for effective permittivity and conductivity mapping of biological scenarios via segmented contrast source inversion," *Prog. Electromagn. Res.*, vol. 164, pp. 1–15, 2019.
[8] M. T. Bevacqua, S. Di Meo, L. Crocco, T. Isernia, and M. Pasian, "Millimeter-waves breast cancer imaging via inverse scattering techniques," *IEEE J. Electromagn., RF Microw. Med. Biol.*, vol. 5, no. 3, pp. 246–253, Sep. 2021.
[9] I. Iliopoulos, S. D. Meo, M. Pasian, M. Zhadobov, P. Pouliguen, P. Potier, L. Perregrini, R. Sauleau, and M. Ettorre, "Enhancement of penetration of millimeter waves by field focusing applied to breast cancer detection," *IEEE Trans. Biomed. Eng.*, vol. 68, no. 3, pp. 959–966, Mar. 2021.
[10] M. T. Bevacqua, G. G. Bellizzi, L. Crocco, and T. Isernia, "A method for quantitative imaging of electrical properties of human tissues from only amplitude electromagnetic data," *Inverse Problems*, vol. 35, no. 2, Feb. 2019, Art. no. 025006.
[11] M. Lazebnik, D. Popovic, L. McCartney, C. B. Watkins, M. J. Lindstrom, J. Harter, S. Sewall, T. Ogilvie, A. Magliocco, T. M. Breslin, W. Temple, D. Mew, J. H. Booske, M. Okoniewski, and S. C. Hagness, "A large-scale study of the ultrawideband microwave dielectric properties of normal, benign and malignant breast tissues obtained from cancer surgeries," *Phys. Med. Biol.*, vol. 52, no. 20, pp. 6093–6115, Oct. 2007.
[12] J. Bourqui and E. C. Fear, "System for bulk dielectric permittivity estimation of breast tissues at microwave frequencies," *IEEE Trans. Microw. Theory Techn.*, vol. 64, no. 9, pp. 3001–3009, Sep. 2016.
[13] R. Scapaticci, M. Bjelogrlic, J. A. Tobon Vasquez, F. Vipiana, M. Mattes, and L. Crocco, "Microwave technology for brain imaging and monitoring: Physical foundations, potential and limitations," in *Emerging Electromagnetic Technologies for Brain Diseases Diagnostics, Monitoring and Therapy*. Springer, 2018, pp. 7–35.
[14] R. Scapaticci, L. Di Donato, I. Catapano, and L. Crocco, "A feasibility study on microwave imaging for brain stroke monitoring," *Prog. Electromagn. Res. B*, vol. 40, pp. 305–324, 2012.

[15] J. A. Tobon Vasquez, R. Scapaticci, G. Turvani, G. Bellizzi, D. O. Rodriguez-Duarte, N. Joachimowicz, B. Duchune, E. Tedeschi, M. R. Casu, L. Crocco, and F. Vipiana, "A prototype microwave system for 3D brain stroke imaging," *Sensors*, vol. 20, no. 9, p. 2607, May 2020.

[16] S. Y. Semenov, A. E. Bulyshev, V. G. Posukh, Y. E. Sizov, T. C. Williams, and A. E. Souvorov, "Microwave tomography for detection/imaging of myocardial infarction. I. Excised canine hearts," *Ann. Biomed. Eng.*, vol. 31, no. 3, pp. 262–270, Mar. 2003.

[17] S. A. Khan, A. A. Khan, and M. Tariq, "Temperature dependence of relative permittivity and dielectric dissipation factor of nano-modified mineral oil for use as insulating liquids in transformers," in *Proc. IEEE Electr. Insul. Conf. (EIC)*, Jun. 2021, pp. 313–316.

[18] P. M. Meaney, D. Goodwin, A. H. Golnabi, T. Zhou, M. Pallone, S. D. Geimer, G. Burke, and K. D. Paulsen, "Clinical microwave tomographic imaging of the calcaneus: A first-in-human case study of two subjects," *IEEE Trans. Biomed. Eng.*, vol. 59, no. 12, pp. 3304–3313, Dec. 2012.

[19] J. E. Fajardo, F. P. Lotto, F. Vericat, C. M. Carlevaro, and R. M. Irastorza, "Microwave tomography with phaseless data on the calcaneus by means of artificial neural networks," *Med. Biol. Eng. Comput.*, vol. 58, no. 2, pp. 433–442, Feb. 2020.

[20] B. Amin, A. Shahzad, L. Farina, E. Parle, L. McNamara, M. O'Halloran, and M. A. Elahi, "Dielectric characterization of diseased human trabecular bones at microwave frequency," *Med. Eng. Phys.*, vol. 78, pp. 21–28, Apr. 2020.

[21] B. Amin, A. Shahzad, L. Crocco, M. Wang, M. O'Halloran, A. González-Suárez, and M. A. Elahi, "A feasibility study on microwave imaging of bone for osteoporosis monitoring," *Med. Biol. Eng. Comput.*, vol. 59, no. 4, pp. 925–936, Apr. 2021.

[22] *Bone Health and Osteoporosis: A Report of the Surgeon General*, U.S. Dept. Health Human Services, Washington, DC, USA, 2004, pp. 228–437.

[23] B. Amin, A. Shahzad, M. O'halloran, B. Mcdermott, and A. Elahi, "Experimental validation of microwave imaging prototype and DBIM-IMATCS algorithm for bone health monitoring," *IEEE Access*, vol. 10, pp. 42589–42600, 2022.

[24] E.-M. Lochmüller, R. Müller, V. Kuhn, C. A. Lill, and F. Eckstein, "Can novel clinical densitometric techniques replace or improve DXA in predicting bone strength in osteoporosis at the hip and other skeletal sites?" *J. Bone Mineral Res.*, vol. 18, no. 5, pp. 906–912, May 2003.

[25] P. M. Meaney, T. Zhou, D. Goodwin, A. Golnabi, E. A. Attardo, and K. D. Paulsen, "Bone dielectric property variation as a function of mineralization at microwave frequencies," *Int. J. Biomed. Imag.*, vol. 2012, pp. 1–9, Jun. 2012.

[26] C. Gilmore, A. Abubakar, W. Hu, T. M. Habashy, and P. M. van den Berg, "Microwave biomedical data inversion using the finite-difference contrast source inversion method," *IEEE Trans. Antennas Propag.*, vol. 57, no. 5, pp. 1528–1538, May 2009.

[27] R. Scapaticci, I. Catapano, and L. Crocco, "Wavelet-based adaptive multiresolution inversion for quantitative microwave imaging of breast tissues," *IEEE Trans. Antennas Propag.*, vol. 60, no. 8, pp. 3717–3726, Aug. 2012.

[28] P. M. Meaney, M. W. Fanning, T. Raynolds, C. J. Fox, Q. Fang, C. A. Kogel, S. P. Poplack, and K. D. Paulsen, "Initial clinical experience with microwave breast imaging in women with normal mammography," *Academic Radiol.*, vol. 14, no. 2, pp. 207–218, Feb. 2007.

[29] J. D. Shea, P. Kosmas, S. C. Hagness, and B. D. Van Veen, "Three-dimensional microwave imaging of realistic numerical breast phantoms via a multiple-frequency inverse scattering technique," *Med. Phys.*, vol. 37, no. 8, pp. 4210–4226, Aug. 2010.

[30] M. Azghani, P. Kosmas, and F. Marvasti, "Microwave medical imaging based on sparsity and an iterative method with adaptive thresholding," *IEEE Trans. Med. Imag.*, vol. 34, no. 2, pp. 357–365, Feb. 2015.

[31] B. Amin, A. Shahzad, M. O'Halloran, and M. A. Elahi, "Microwave bone imaging: A preliminary investigation on numerical bone phantoms for bone health monitoring," *Sensors*, vol. 20, no. 21, p. 6320, Nov. 2020.

[32] Z. Miao and P. Kosmas, "Multiple-frequency DBIM-TwIST algorithm for microwave breast imaging," *IEEE Trans. Antennas Propag.*, vol. 65, no. 5, pp. 2507–2516, May 2017.

[33] L. M. Neira, B. D. Van Veen, and S. C. Hagness, "High-resolution microwave breast imaging using a 3-D inverse scattering algorithm with a variable-strength spatial prior constraint," *IEEE Trans. Antennas Propag.*, vol. 65, no. 11, pp. 6002–6014, Nov. 2017.

[34] C. Gilmore, A. Zakaria, S. Pistorius, and J. LoVetri, "Microwave imaging of human forearms: Pilot study and image enhancement," *Int. J. Biomed. Imag.*, vol. 2013, Jul. 2013, Art. no. 673027.

[35] V. Zhurbenko, "Challenges in the design of microwave imaging systems for breast cancer detection," *Adv. Electr. Comput. Eng.*, vol. 11, no. 1, pp. 91–96, 2011.

[36] I. Catapano, L. Di Donato, L. Crocco, O. M. Bucci, A. F. Morabito, T. Isernia, and R. Massa, "On quantitative microwave tomography of female breast," *Prog. Electromagn. Res.*, vol. 97, pp. 75–93, 2009.

[37] M. Alkhodari, A. Zakaria, and N. Qaddoumi, "Monitoring bone density using microwave tomography of human legs: A numerical feasibility study," *Sensors*, vol. 21, no. 21, p. 7078, Oct. 2021.

[38] M. Ambrosanio, P. Kosmas, and V. Pascazio, "A multithreshold iterative DBIM-based algorithm for the imaging of heterogeneous breast tissues," *IEEE Trans. Biomed. Eng.*, vol. 66, no. 2, pp. 509–520, Feb. 2019.

[39] B. Khalesi, B. Sohani, N. Ghavami, M. Ghavami, S. Dudley, and G. Tiberi, "Free-space operating microwave imaging device for bone lesion detection: A phantom investigation," *IEEE Antennas Wireless Propag. Lett.*, vol. 19, pp. 2393–2397, 2020.

[40] K. C. Santos, C. A. Fernandes, and J. R. Costa, "Validation of a compact microwave imaging system for bone fracture detection," *IEEE Access*, vol. 11, pp. 63690–63700, 2023.

[41] Y. Jiang, M. Liu, and T. Li, "Feasibility analysis of bone abnormality diagnosis based on microwave technology," in *Proc. 3rd Int. Conf. Comput. Vis., Image Deep Learn. Int. Conf. Comput. Eng. Appl. (CVIDL ICCEA)*, Changchun, China, May 2022, pp. 926–930.

[42] A. Cannata, A. Shahzad, M. O'Halloran, A. Elahi, M. Pasian, S. Di Meo, G. Matrone, and B. Amin, "Numerical assessment of microwave bone imaging: Reconstruction of realistic phantoms for diagnosing different bone diseases," in *Proc. 24th Int. Conf. Appl. Electromagn. Commun. (ICECOM)*, Sep. 2023, pp. 27–29.

[43] A. Cannata, A. Elahi, M. O'Halloran, M. Pasian, S. Di Meo, G. Matrone, and B. Amin, "Microwave tomography bone imaging: Analysing the impact of skin thickness on the reconstruction of numerical bone phantoms," in *Proc. 18th Eur. Conf. Antennas Propag. (EuCAP)*, Mar. 2024, pp. 17–22.

[44] S. Gabriel, R. W. Lau, and C. Gabriel, "The dielectric properties of biological tissues: III. parametric models for the dielectric spectrum of tissues," *Phys. Med. Biol.*, vol. 41, no. 11, pp. 2271–2293, Nov. 1996.

[45] Z. Wang, A. C. Bovik, H. R. Sheikh, and E. P. Simoncelli, "Image quality assessment: From error visibility to structural similarity," *IEEE Trans. Image Process.*, vol. 13, no. 4, pp. 600–612, Apr. 2004.

[46] C. Gabriel, "Dielectric properties of body tissues in the frequency range 10Hz–100GHz," L'Istituto di Fisica Applicata 'Nello Carrara' (IFAC), 2010.

ALESSIA CANNATÀ (Member, IEEE) was born in Milan, Italy, in 1996. She received the B.S. and M.Sc. degrees in bioengineering from the University of Pavia, Pavia, Italy, in 2019 and 2021, respectively, where she is currently pursuing the Ph.D. degree. She graduated with a thesis concerning the dielectric and mechanical characterization of bi-modal tissue-mimicking phantoms. She has been with the Microwave Laboratory and the Bioengineering Laboratory, Department of Electrical, Computer, and Biomedical Engineering. Since 2023, she spent five months in Galway, Ireland, working at the Translational Medical Device Laboratory, University of Galway thanks to an Erasmus+ Traineeship Programme. Her current research interests include microwave imaging, multi-modal characterization, and imaging algorithms.

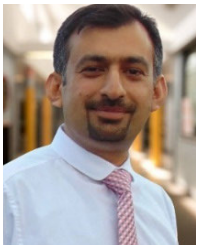

ADNAN ELAHI (Member, IEEE) received the B.S. degree in computer engineering from COMSATS University, Pakistan, the M.Sc. degree in embedded digital systems from the University of Sussex, U.K., and the M.Sc. degree in data analytics and the Ph.D. degree in electronic engineering from the University of Galway. He is currently a Lecturer in medical electronics and the Co-Director of the Translational Medical Device Laboratory, University of Galway. His Ph.D. research focused on investigating and developing novel signal-processing algorithms to improve microwave imaging of the breast. His current research spans the disciplines of engineering and medicine, with a particular focus on smart devices for remote patient monitoring, novel and personalized therapeutics using RF/microwave and pulsed-field ablation, and AI/machine learning for biomedical signals.

MARTIN O'HALLORAN received the B.E. degree in electronic and computer engineering and the Ph.D. degree in electrical engineering from the University of Galway, in 2004 and 2009, respectively. He is currently a Full Professor of medical electronics with the University of Galway, with a research focus on applied medical device development. In parallel, he leads Ireland's Bioinnovate program, a sister program of Stanford's Biodesign. Finally, he is a seven-time recipient of funding from European Research Council (ERC).

MARCO PASIAN (Senior Member, IEEE) was born in 1980. He received the M.Sc. degree (cum laude) in electronic engineering and the Ph.D. degree in electronics and computer science from the University of Pavia, Pavia, Italy, in 2005 and 2009, respectively.

From 2004 to 2008, he spent periods with European Space Agency, Darmstadt, Germany, the Carlo Gavazzi Space, Milan, Italy, and the TNO, Defense, Security and Safety, The Hague, The Netherlands. From 2009 to 2013, he was a Postdoctoral Researcher with the Microwave Laboratory, University of Pavia, where he was an Assistant Professor, from 2013 to 2020, and has been an Associate Professor, since 2020. He has been a Principal Investigator, or Unit Coordinator, for several competitive European and Italian grants. In addition, he has also been a Project Manager, a Scientific Manager, and a Consultant for several projects in collaborations with European and Italian research centers and industries, including European Space Agency. His research interests include microwave and millimeter wave components, systems, and technologies, including substrate integrated waveguides, for space applications and investigation of complex, nonstandard media, most notably for biomedical imaging and cryosphere monitoring.

Prof. Pasian is a member of European Microwave Association (EuMA) and Italian Society on Electromagnetism (SIEm). He was the Technical Program Committee (TPC) Chair at European Microwave Conference 2022, and served as the TPC Co-Chair, a TPC Member, the Conference Prize Committee Chair, and the Finance Chair for other IEEE and EuMA Conferences. He is an Associate Editor of IEEE JOURNAL OF ELECTROMAGNETICS, RFAND MICROWAVES IN MEDICINE AND BIOLOGY and the Editor-in-Chief of *EuMA International Journal of Microwave and Wireless Technologies*.

SIMONA DI MEO (Member, IEEE) was born in 1992. She received the M.Sc. degree (cum laude) in electronic engineering and the Ph.D. degree in electronics and computer science from the University of Pavia, Pavia, Italy, in 2016 and 2020, respectively.

She is currently an Assistant Professor with both the Microwave Laboratory and the Bioengineering Laboratory, University of Pavia. Her current research interests include innovative techniques for early breast cancer detection. She was the Co-Principal Investigator (Co-PI) with the University of Pavia funding BlueSky Research Project MULTIWAVE.

Dr. Meo was a member of the Technical Program Committee for the Mediterranean Microwave Symposium 2022, and Student Activity Chair for the European Microwave Week 2022. She was the Education and Research Cooperation Committee Chair. She is a member of the IEEE AP-S, MTT-S, EMB-S, WiE, Italian Society on Electromagnetism (SIEm), and a member of the National Group of Bioengineering (GNB). She was a recipient of several awards and recognitions, including the IEEE AP-S Eugene F. Knott Memorial Pre-Doctoral Research Award, in 2015, the IEEE AP-S Doctoral Research Grant in 2018, the IEEE AP-S Fellowship in 2022, and several Young Scientist Awards in the framework of URSI conferences. She is Associate Editor of the *IET Healthcare Technology Letters* and the Editorial Board Member of IEEE OPEN JOURNAL OF ENGINEERING IN MEDICINE AND BIOLOGY.

GIULIA MATRONE (Member, IEEE) was born in Pavia, Italy, in 1985. She received the B.Sc. and M.Sc. degrees (cum laude) in biomedical engineering, and the Ph.D. degree in bioengineering and bioinformatics from the University of Pavia, Pavia, in 2006, 2008, and 2012, respectively.

She is currently an Associate Professor of bioengineering with the Department of Electrical, Computer, and Biomedical Engineering, University of Pavia, where she leads research activities on diagnostic ultrasound and microwave image formation techniques within the Bioengineering Laboratory Group. Her research interests include ultrasound medical imaging, beamforming methods, ultrasound simulation, micro/millimeter-wave imaging for biomedical applications, biomedical signal, and image processing.

Prof. Matrone is a member of the IEEE EMB and IEEE UFFC Societies, and Italian National Group of Bioengineering (GNB). She was an Associate Editor of IEEE ACCESS, from 2019 to 2022. She has been a member of the IEEE International Ultrasonics Symposium Technical Program Committee, since 2020.

BILAL AMIN received the B.S. degree (Hons.) in electrical engineering from COMSATS University Lahore, Pakistan, in 2013, the master's degree (Hons.) in electrical engineering from COMSATS University Islamabad, Pakistan, in 2015, and the Ph.D. degree in electrical and electronics engineering from the University of Galway, Ireland, under the auspices of the National ICT Scholarship Program. He is currently a Postdoctoral Researcher with the School of Medicine, University of Galway, Ireland. His main research interests include bioelectromagnetics in healthcare, with particular attention to microwave bone imaging, dielectric characterization of biological tissues, cardiac implant antenna design, microwave ablation antenna design, and medical signal processing with an academic background in clinical and biomedical engineering. He has received more than 12 national and international awards and is a member of European Cooperation in Science and Technology (COST) Action MiMED and COST Action EMF-MED.